Supporting Information

Peng et al. 10.1073/pnas.1410114111

SI Materials and Methods

SHAPE Footprinting. Complexes of *E. coli* Hfq protein, *rpoS301* RNA, and DsrA sRNA were assembled in 10 μL annealing buffer (50 mM Tris·HCl, pH 7.5, 50 mM NaCl, 50 mM KCl, 50 mM NH_4Cl, 2% glycerol) at 25 °C for 2 h. Reactions contained 50 nM *rpoS301* plus 200 nM DsrA and 333 nM Hfq hexamer as stated in the text. Complexes were modified for 2 h at 37 °C with 1 μL 20 mM *N*-methylisatoic anhydride (Molecular Probes) dissolved in anhydrous DMSO and then analyzed by reverse transcription as previously described (1). cDNA products were quantified using SAFA (2) and normalized to reference bands that showed constant intensity in different lanes of the gel (3). The SHAPE reactivity of *rpoS* RNA complexes relative to *rpoS* RNA alone was calculated from the ratios of adjusted band intensities and ranged from 0.15 to 8.88 (Fig. S1*D*). Outliers with values 30–100 times above the background usually occurred next to very strong RT pauses and were manually excluded from the data. Each SHAPE reactivity profile is the average of at least three independent experiments. Error bars represent the SD from the mean. A histogram for the entire dataset was constructed with bin sizes equal to the average SD of the SHAPE reactivity, and the nucleotides were grouped and colored as illustrated in Fig. S1*D*. Secondary structure schemes were prepared with xrna (rna.ucsc.edu/rnacenter/xrna/xrna.html).

SAXS. Hfq was purified as previously described (4). Concentrated protein was dialyzed twice against SAXS buffer (annealing buffer plus 2 mM $MgCl_2$) at a final concentration of 1.90 mg/mL (170 μM monomer). *rpoS301* RNA was purified by a native 6% polyacrylamide gel in 1× THEM2, eluted from the gel overnight at 4 °C in SAXS buffer, concentrated by ultrafiltration (Amicon Ultra-15 centrifugal filter unit, 50 kDa), and washed five times with fresh SAXS buffer (5). The final concentration was 0.43 mg/mL (4.6 μM). Samples were shipped on ice and stored at 4 °C before use. Remaining SAXS buffer from the sample preparation was used for diluting samples and measuring background scattering. Small-angle X-ray scattering data were collected at the Advanced Photon Source 12-ID-B, over the range $0.005 < q < 1.007$ $Å^{-1}$ as described previously (5). Guinier fits and real space inversions were done using Primus and GNOM from the ATSAS software package (6). Other plots were generated using the ScÅtter software package (bl1231.als.lbl.gov/scatter). SAXS data collected on fresh samples with different concentrations showed constant R_g and ratios of scattering intensity, indicating a lack of interparticle interactions (Fig. S4), although dynamic light scattering of frozen samples showed ∼11% scattering from an RNA dimer. Estimates of the molecular mass by the method of Rambo and Tainer (7) were within 10% of the nominal value (Table S2). The disordered C terminus of Hfq may result in higher than expected estimates by this method (8).

MC-Sym. Three-dimensional models of *rpoS* mRNA secondary structure fragments (Fig. S7) were generated using MC-Sym web server (9). The RNA sequence and secondary structure based on SHAPE experiments were used as the input with default settings; two-stranded fragments were first connected with a GAAA tetraloop. The output structures were ranked using the MC-Sym web server tools. The top five predicted structures for each fragment did not differ substantially. The highest-scoring structure for each fragment was selected for rigid-body modeling, after removal of GAAA tetraloops and energy minimization with UCSF Chimera (10). The predicted structures were consistent with the experimental SHAPE data, with highly modified residues occurring in hairpin loops or kinks in the RNA backbone (Fig. S7). The "hinge" region of the structure (light blue in Fig. S7) is the least well determined, but even the model for this region is in reasonable agreement with the data. The two three-helix junctions (type C) (11) were also predicted using a knowledge-based method (12–14). This method returned the same stacking geometry as in our model for the inhibitory stem-loop domain (pink in Fig. S7), but a slightly different stacking geometry for the upstream three-helix junction (red in Fig. S7).

Rigid-Body Modeling of *rpoS* and *rpoS*•Hfq Complex. The tertiary structure of *rpoS* RNA was modeled by orienting the RNA fragments by rigid-body modeling (SASREF) (15), using the SAXS experimental data as a constraint ($\chi^2 = 0.59$). The RNA connectivity was enforced by setting the distance between adjacent phosphorous atoms to ≤7 Å (res 40–41, 57–58, and 127–128). To allow more flexibility in the fitting procedure, the distance between connecting phosphorus atoms was constrained to ≤8 Å in only one of the two strands in the inhibitory stem (res 162–163 or res 272–273 for connecting fragments 4 and 5, and res 184–185 or res 248–249 for connecting fragments 5 and 6). Because we could not model single-stranded regions of the upstream domain (res 73–86 and res 102–116) with MC-Sym, the missing sequences were initially built assuming an A-form conformation, and all of the fragments were manually connected into a continuous strand in UCSF Chimera (10). Structures resulting from repeated calculations were similar, with two structural domains oriented at ∼90°. The predicted structures were not sensitive to changes in distance constraints.

CORAL was used to model the full *rpoS*•Hfq complex against the SAXS data for the 1:1 RNA:Hfq sample (16). An initial model of Hfq core bound to the AAN_4 motif was obtained by importing the coordinates of six protomers of *E. coli* $Hfq_{5–65}$ in complex with A_7 RNA (PDB ID: 4HT8) (17). To this model, we added the missing C termini of Hfq (resi 66–102) and the *rpoS* fragments used for SASREF modeling of free *rpoS* RNA with the same contact restraints. The A7 RNA bound to Hfq was joined to the rest of the RNA by setting the distance between *rpoS301* P 88 and the 3′ end of A7 ≤7 Å. Two additional constraints were introduced based on the SHAPE footprinting data: *rpoS301* P 195 (U_5 motif) ≤12 Å from the α-carbon of R16 in any Hfq monomer and *rpoS301* P157 (inhibitory stem) ≤15 Å from R16 α-carbon in any Hfq monomer. Finally, the missing nucleotides (nucleotides 73–80 and 102–116) were built and connected manually in UCSF Chimera.

Monte Carlo Simulations of Hfq, *rpoS*, and Hfq•*rpoS* Complexes by SASSIE. Monte Carlo simulations (SASSIE) (18) were used to identify conformations of free Hfq, free *rpoS* mRNA, and the *rpoS*•Hfq complex consistent with the scattering data for each sample. The coordinates of the Hfq core (alone or with rA bound to the distal face) (17) were fixed during the simulations, whereas the N- and C-terminal residues (res 1–5 and res 66–102) were allowed to vary. The initial full-length Hfq structure was energy minimized using CHARMM (19), before it was used as the input for the Monte Carlo simulation. During the Monte Carlo simulation, Crysol 2.7 (20) was used to calculate scattering profiles of simulated structures after renaming atoms to C, H, N, O, P, S to avoid reading errors in Crysol. The averaged SAXS profile of Hfq was interpolated (43 points, $\Delta q = 0.005$ from 0.005

to 0.21) and was used to evaluate the theoretical scattering profiles. Models generated by SASSIE that best fitted the experimental SAXS data were minimized using CHARMM.

The free *rpoS* structure generated by rigid-body modeling was modeled using SASSIE as described above. However, the RNA was allowed to pivot around the flexible hinge connecting the upstream and downstream domains (res 128–129). The Monte Carlo dihedral sampling of RNA backbone configurations was carried out using CHARMM 36 force-field parameters (21) for α, β, γ, δ, ε, η angles, using the same energetic sampling as described previously (18).

The RNA coordinates of the *rpoS*•Hfq complex generated from rigid-body modeling and the full-length Hfq structure generated from SASSIE were merged into a starting structure for Monte Carlo simulations of the complex. CHARMM was used to minimize the energy in three steps by first restraining all RNA atoms, then restraining the RNA carbon and phosphate atoms, and then allowing all atoms to move. A SASSIE Monte Carlo simulation was carried out as above, using *rpoS* res 128–129 as a pivot point and allowing Hfq N and C termini to vary. The SAXS profile of the 1:1 *rpoS*•Hfq sample was used to evaluate the theoretical scattering profiles, using χ^2 (Eq. **S1**) as a measure of statistical goodness-of-fit,

$$\chi^2 = \frac{1}{(N-1)} \sum_{Q_i} \frac{\left(I_{\exp}(Q_i) - I_{\mathrm{calc}}(Q_i)\right)^2}{\sigma_{\exp}(Q_i)^2}, \qquad \textbf{[S1]}$$

in which $I_{\exp}(Q_i)$ is the experimentally determined SAXS scattering curve, $I_{\mathrm{calc}}(Q_i)$ is the value obtained using SASSIE, $\sigma_{\exp}(Q_i)$ is the experimentally determined Q-dependent variance, and the sum was taken over $i = 1$ to N, with $n = 43$ grid points of momentum transfer Q. Some values of $\chi^2 < 1$, indicating that either our estimate of $\sigma_{\exp}(Q_i)$ is too large or more likely that the there are fewer than $N - 1$ df in our dataset. To account for variance in the value of χ^2 ($3\sigma \sim \pm 0.66$) given the limited number of data points and the uncertainty in the true number of degrees of freedom in the data, we arbitrarily considered all models with $\chi^2 < 1.5$, which span the experimentally determined R_g value. An alternative measure of error $V(r)$ (7) reached a minimum around a similar range of R_g values (Fig. S6). The best-fit structures were energy minimized using CHARMM. Final models were compared with the scattering data, using FoXS (22).

1. Peng Y, Soper TJ, Woodson SA (2012) RNase footprinting of protein binding sites on an mRNA target of small RNAs. *Methods Mol Biol* 905:213–224.
2. Das R, Laederach A, Pearlman SM, Herschlag D, Altman RB (2005) SAFA: Semi-automated footprinting analysis software for high-throughput quantification of nucleic acid footprinting experiments. *RNA* 11(3):344–354.
3. Behrouzi R (2012) The roles of native tertiary interactions in the folding pathway of the Azoarcus ribozyme. PhD thesis (ProQuest Dissertations and Theses, Johns Hopkins University, Baltimore).
4. Soper TJ, Doxzen K, Woodson SA (2011) Major role for mRNA binding and restructuring in sRNA recruitment by Hfq. *RNA* 17(8):1544–1550.
5. Fang X, et al. (2013) An unusual topological structure of the HIV-1 Rev response element. *Cell* 155(3):594–605.
6. Konarev PV, Volkov VV, Sokolova AV, Koch MHJ, Svergun DI (2003) PRIMUS: A Windows PC-based system for small-angle scattering data analysis. *J Appl Cryst* 36(5):1277–1282.
7. Rambo RP, Tainer JA (2013) Accurate assessment of mass, models and resolution by small-angle scattering. *Nature* 496(7446):477–481.
8. Watson MC, Curtis JE (2014) Probing the average local structure of biomolecules using small-angle scattering and scaling laws. *Biophys J* 106(11):2474–2482.
9. Parisien M, Major F (2008) The MC-Fold and MC-Sym pipeline infers RNA structure from sequence data. *Nature* 452(7183):51–55.
10. Pettersen EF, et al. (2004) UCSF Chimera—a visualization system for exploratory research and analysis. *J Comput Chem* 25(13):1605–1612.
11. Lescoute A, Westhof E (2006) Topology of three-way junctions in folded RNAs. *RNA* 12(1):83–93.
12. Kim N, et al. (2014) Graph-based sampling for approximating global helical topologies of RNA. *Proc Natl Acad Sci USA* 111(11):4079–4084.
13. Laing C, Schlick T (2009) Analysis of four-way junctions in RNA structures. *J Mol Biol* 390(3):547–559.
14. Laing C, Wen D, Wang JT, Schlick T (2012) Predicting coaxial helical stacking in RNA junctions. *Nucleic Acids Res* 40(2):487–498.
15. Petoukhov MV, Svergun DI (2005) Global rigid body modeling of macromolecular complexes against small-angle scattering data. *Biophys J* 89(2):1237–1250.
16. Petoukhov MV, et al. (2012) New developments in the ATSAS program package for small-angle scattering data analysis. *J Appl Cryst* 45(2):342–350.
17. Wang W, et al. (2011) Cooperation of Escherichia coli Hfq hexamers in DsrA binding. *Genes Dev* 25(19):2106–2117.
18. Curtis JE, Raghunandan S, Nanda H, Krueger S (2012) SASSIE: A program to study intrinsically disordered biological molecules and macromolecular ensembles using experimental scattering restraints. *Comput Phys Commun* 183(2):382–389.
19. Brooks BR, et al. (2009) CHARMM: The biomolecular simulation program. *J Comput Chem* 30(10):1545–1614.
20. Svergun DI, Barberato C, Koch MHJ (1995) CRYSOL - a program to evaluate X-ray solution scattering of biological macromolecules from atomic coordinates. *J Appl Cryst* 28:768–773.
21. Foloppe N, MacKerell JAD (2000) All-atom empirical force field for nucleic acids: I. Parameter optimization based on small molecule and condensed phase macromolecular target data. *J Comput Chem* 21(2):86–104.
22. Schneidman-Duhovny D, Hammel M, Tainer JA, Sali A (2013) Accurate SAXS profile computation and its assessment by contrast variation experiments. *Biophys J* 105(4):962–974.

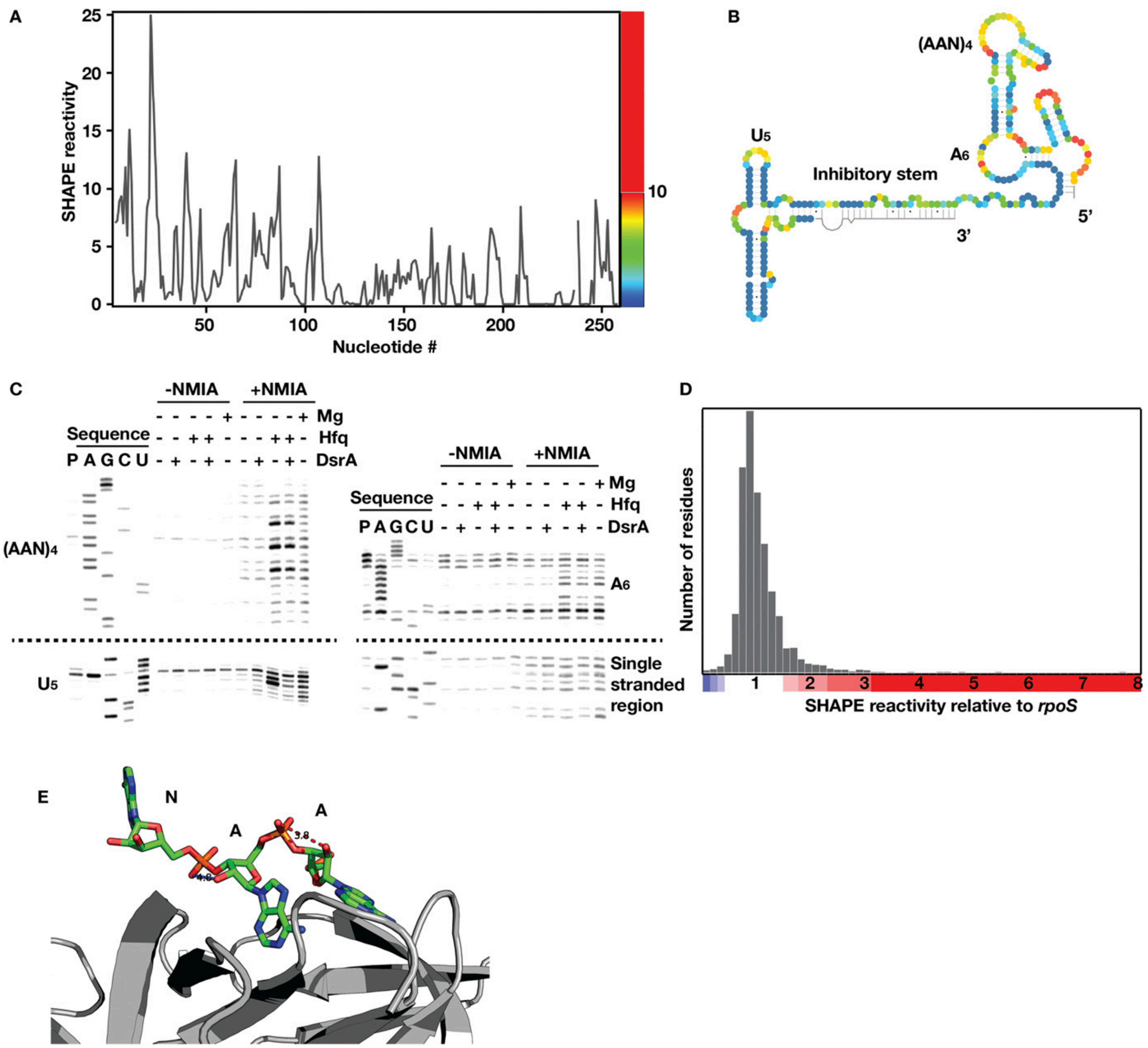

Fig. S1. SHAPE footprinting of *rpoS* mRNA with sRNA and Hfq. (*A*) Modification of ribose 2′OH was quantified by primer extension and analyzed by sequencing gel electrophoresis. To determine the overall secondary structure, traces from primer extensions covering different regions of the *rpoS301* RNA were overlapped. (*B*) rpoS301 secondary structure consistent with experimental SHAPE modification data (colors). The linker between the upstream and downstream domains is predicted by MC-Sym to fold into a short stem loop, in agreement with its low reactivity. Gray, no data. (*C*) Selected sequencing gel images showing hyperreactive residues induced by Hfq binding at the (AAN)$_4$ motif (*Top Left*) and the U$_5$ motif (*Bottom Left*). Hfq also opens the secondary structure at the A$_6$ motif (*Top Right*) but does not affect other single-stranded regions (*Bottom Right*). (*D*) Histogram of SHAPE reactivity relative to *rpoS* RNA for the entire dataset. Values below 0.6 (~3% of nucleotides) were considered protected; values above 1.75 were considered enhanced (~10% of nucleotides). Nucleotides were clustered based on their relative SHAPE reactivity: dark to light blue, protected, 0.140–0.287 (~0.2%), 0.287–0.434 (~0.3%), and 0.434–0.581 (~0.6%); white, unchanged, 0.728–1.757 (~87.1%); and light to dark red, enhanced, 1.757–2.051 (~4.5%), 2.051–2.639 (~3.4%), 2.639–3.521 (~1.5%), and 3.521–8.813 (~0.8%). RNA secondary structure schematics were drawn with XRNA (rna.ucsc.edu/rnacenter/xrna/xrna.html). (*E*) Structure of AAN triple bound to the distal face of Hfq (PDB ID: 3GIB) showing the short 3.8-Å distance between the first 2′OH and the phosphate of the second A. This conformation is associated with strong reactivity toward electrophiles used for SHAPE chemistry (1).

1. Steen KA, Rice GM, Weeks KM (2012) Fingerprinting noncanonical and tertiary RNA structures by differential SHAPE reactivity. *J Am Chem Soc* 134(32):13160–13163.

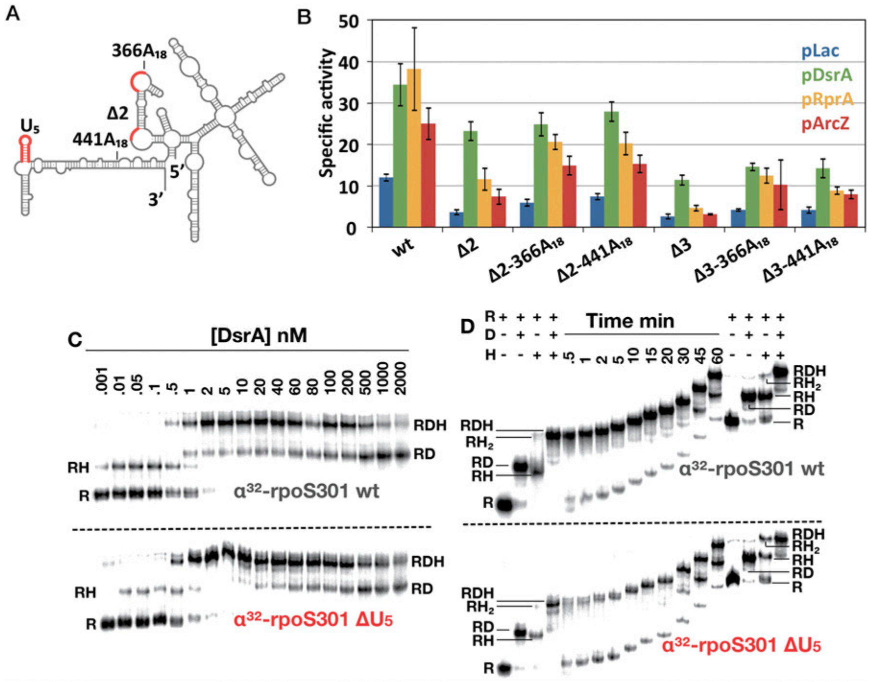

Fig. S2. The U5 motif functions independently of the AAN motif. (*A* and *B*) Full-length *rpoS* leader (576 nt) fused to *lacZ* was used to measure in vivo expression of β-galactosidase as in Fig. 3*B*. Δ2, upstream $(AAN)_4$ and A_6 motifs were replaced with GC-rich sequence (1); Δ3, ΔU_5 plus Δ2 mutation; $366A_{18}$ and $441A_{18}$, an A18 insertion at positions 366 and 441 to rescue Δ2 *rpoS* function (2). (*C* and *D*) Native polyacrylamide gel mobility shift assay for DsrA binding to rpoS mRNA. (*C*) Equilibrium binding at different DsrA concentrations. Fraction bound was calculated from counts in each lane in *rpoS*•DsrA (RD) or *rpoS*•DsrA•Hfq (RDH) bands. (*D*) Binding kinetics, as in *C*. Samples were loaded at various times during electrophoresis.

1. Soper T, Mandin P, Majdalani N, Gottesman S, Woodson SA (2010) Positive regulation by small RNAs and the role of Hfq. *Proc Natl Acad Sci USA* 107(21):9602–9607.
2. Peng Y, Soper TJ, Woodson SA (2014) Positional effects of AAN motifs in rpoS regulation by sRNAs and Hfq. *J Mol Biol* 426(2):275–285.

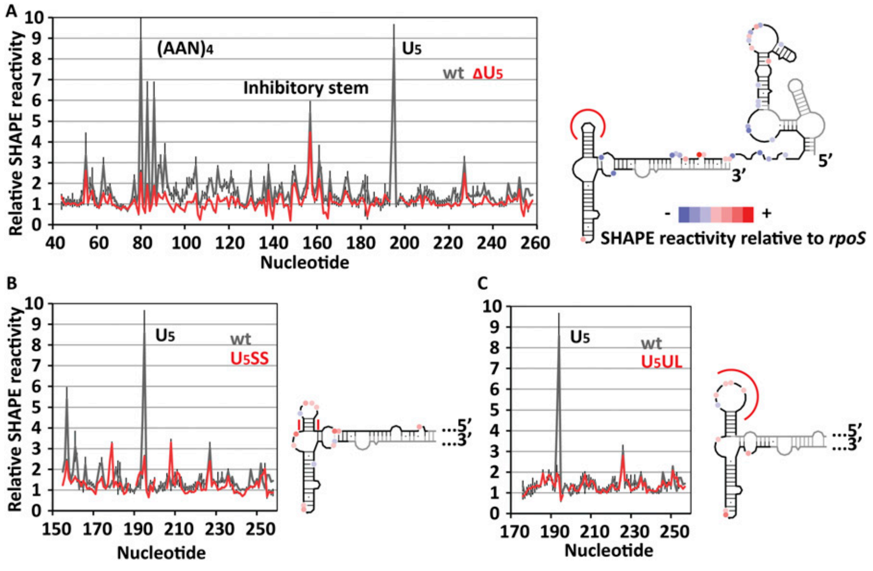

Fig. S3. (*A*–*C*) Hfq specifically recognizes the U_5 motif. Shown is comparison of relative SHAPE reactivity of WT *rpoS*•Hfq complex (gray trace) and U_5 mutant *rpoS*•Hfq complexes (red trace). Mutations (highlighted in red lines) are as shown in Fig. 3*A*. These mutations were predicted by MFOLD (1) not to alter the rest of the RNA secondary structure.

1. Zuker M (2003) Mfold web server for nucleic acid folding and hybridization prediction. *Nucleic Acids Res* 31(13):3406–3415.

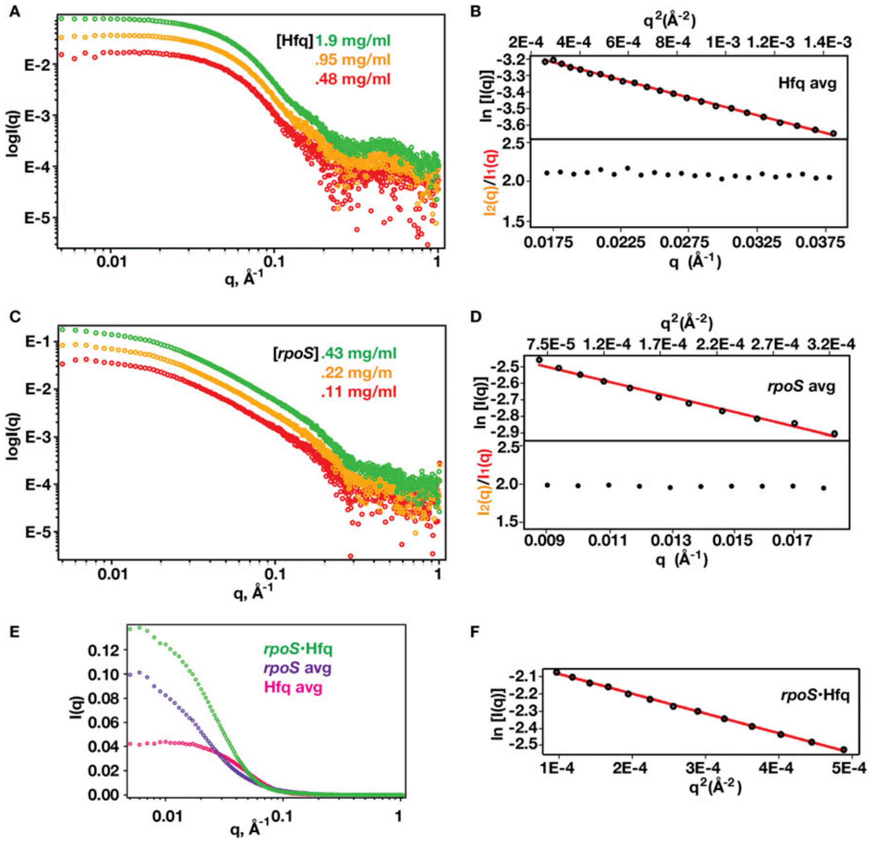

Fig. S4. Solution scattering of Hfq and *rpoS* mRNA. Shown are SAXS scattering profiles of (*A* and *B*) full-length Hfq and (*C* and *D*) *rpoS301* RNA at three concentrations (colored green, orange, and red) in solution. (*B* and *D*, *Top*) Guinier plot of averaged data for free Hfq and free *rpoS*301 RNA. (*Bottom*) The ratio of scattering intensity from two Hfq or RNA concentrations remained constant over the Guinier region, confirming the absence of interparticle interactions (shown here for the lowest two concentrations that differ by a factor of 2). (*E*) The averaged scattering curves for Hfq (magenta), *rpoS* RNA (purple), and 1:1 *rpoS*•Hfq complex (green) were used to calculate R_g from the Guinier region (33.6 ± 0.5 Å, 68.1 ± 1.6 Å, and 58.0 ± 1.0 Å, respectively). (*F*) Guinier plot of 1:1 *rpoS*•Hfq complex.

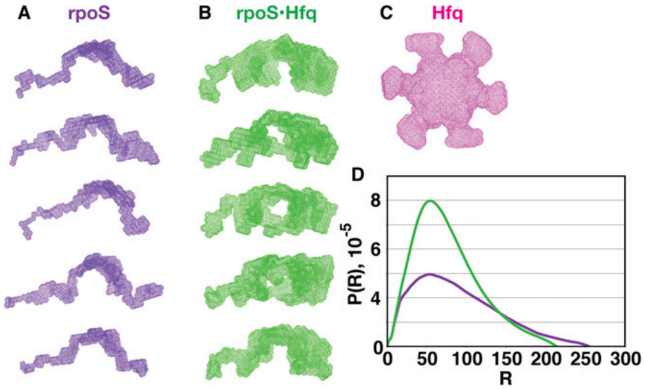

Fig. S5. Ab initio models of *rpoS* RNA, Hfq protein, and the *rpoS*•Hfq complex. (*A* and *B*) Five ab initio structures predicted by DAMMIF for (*A*) free *rpoS* RNA and (*B*) the *rpoS*•Hfq complex (1:1 molar ratio). The *rpoS* envelopes adopt an extended L-shaped conformation, consistent with the all-atom model (Fig. 5). Hfq binding folds *rpoS* RNA into a more compact conformation. DAMMIF assumes the electron density is evenly distributed in the complex and does not account for differential SAXS scattering intensity from Hfq protein and *rpoS* mRNA. As a result, the space occupied by Hfq protein appears empty in the molecular envelope. Averaging these ab initio models resulted in a significant loss of structural detail. (*C*) The averaged ab initio model of Hfq predicted by DAMAVER (1) is very similar to previous models based on SAXS data (2, 3), which assumed oblate P6 symmetry. Twenty DAMMIF bead models were averaged and DAMMIN was restarted to fit the experimental data. (*D*) *P*(*R*) distribution of free *rpoS* RNA (purple) and the *rpoS*•Hfq complex (green), showing the change in the average conformation of the particle. The mass of the RNA and Hfq particles was calculated from the molecular volume, Vc, using the method of Rambo and Tainer (4). Real space parameters for the scattering data are given in Table S2.

1. Volkov VV, Svergun DI (2003) Uniqueness of ab initio shape determination in small-angle scattering. *J Appl Cryst* 36(3 Part 1):860–864.
2. Beich-Frandsen M, Večerek B, Sjöblom B, Bläsi U, Djinović-Carugo K (2011) Structural analysis of full-length Hfq from Escherichia coli. *Acta Crystallogr Sect F Struct Biol Cryst Commun* 67 (Pt 5):536–540.
3. Henderson CA, et al. (2013) Hfq binding changes the structure of Escherichia coli small noncoding RNAs OxyS and RprA, which are involved in the riboregulation of rpoS. *RNA* 19(8): 1089–1104.
4. Rambo RP, Tainer JA (2013) Accurate assessment of mass, models and resolution by small-angle scattering. *Nature* 496(7446):477–481.

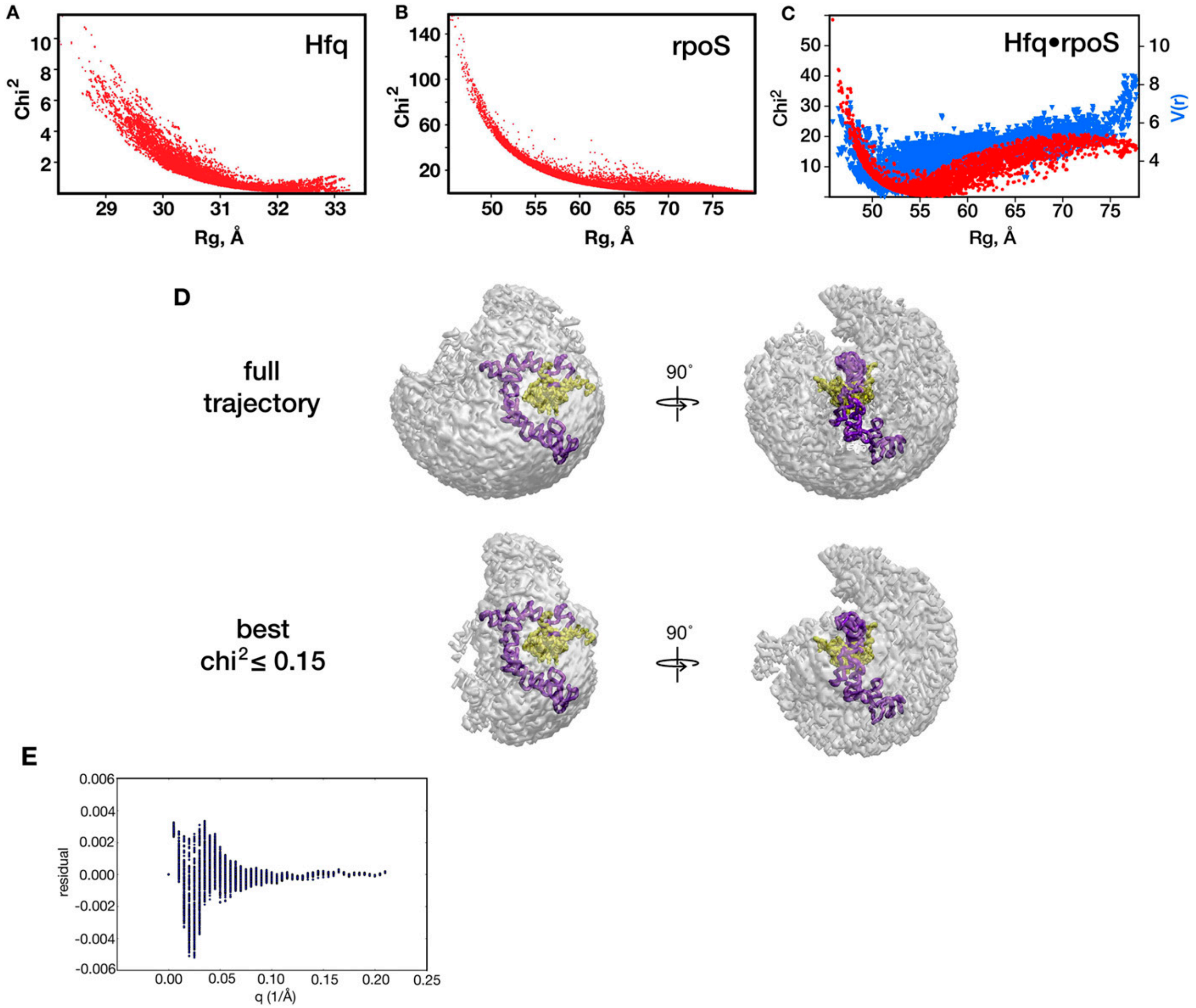

Fig. S6. Monte Carlo and molecular dynamics simulations of free Hfq and *rpoS* RNA. (*A*–*C*) Comparison of experimental SAXS data with Monte Carlo simulations of (*A*) Hfq (24,991 structures), (*B*) free *rpoS* mRNA (27,427 structures), and (*C*) *rpoS*•Hfq complex (19,132 structures), performed with the program SASSIE (18). In *A*, the conformations of the intrinsically disordered N- and C-terminal residues were varied until the space around the hexamer core was fully sampled. (*B* and *C*) Residues 128–129 were used as a pivot point to produce an ensemble of structures spanning the experimental R_g for the free RNA (68.1 Å) and the complex (58 Å). The metric *Vr* (7) (blue in *C*) reaches a minimum at similar R_g values to χ^2, but is less sensitive to variations in the structures. The "best-fit" structure in this ensemble is depicted as an example of the "open" conformation of the *rpoS*•Hfq complex (Fig. 5*E*). (*D*) Spatial distribution of downstream *rpoS* mRNA domain in simulated Hfq•*rpoS* RNA structures (gray surface). Models were aligned to Hfq and superimposed. One conformation in the trajectory is shown as a ribbon; RNA, violet; Hfq, yellow. (*Top*) In the full trajectory, the downstream *rpoS* mRNA domain sampled the entire space around the Hfq Sm core. (*Bottom*) Structures that best match the experimental SAXS data ($\chi^2 \leq 1.5$) are confined to a wedge of space around the proximal face of Hfq, as also shown in Fig. 5*G*. (*E*) A plot of the residual (calculated profile minus experimental profile) for each of the 917 structures of the complex with $\chi^2 \leq 1.5$. Although some positive serial correlation was observed (Durbin–Watson statistical test <2), the magnitude of the residuals was on the order of the statistical error of the data.

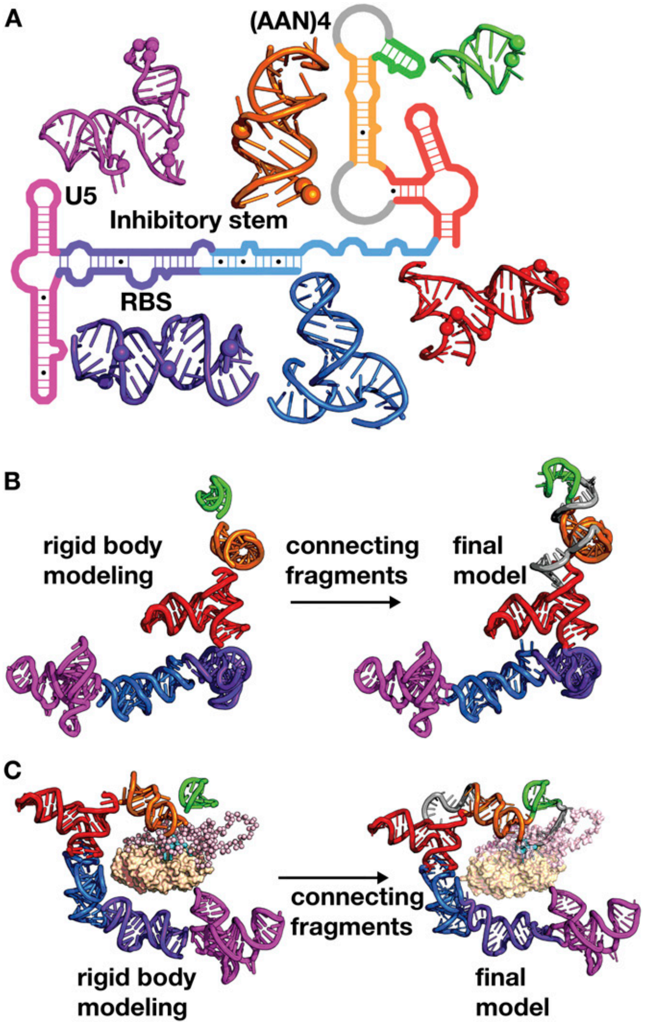

Fig. S7. Tertiary structures of rpoS301 fragments predicted by MC-Sym. (*A*) Using the SHAPE-determined secondary structure as a guide (Fig. S1), *rpoS301* was divided into six fragments. The tertiary structure of each fragment was predicted by MC-Sym (9): an upstream four-way junction (red), a long helix connecting the $(AAN)_4$ motif and A_6 loops (orange), a short hairpin next to the $(AAN)_4$ motif (green), a linker region (blue), the inhibitory stem (purple), and the downstream four-way junction containing the U_5 motif (magenta). The single-stranded $(AAN)_4$ and A_6 motifs were assumed to be unstructured linkers, based on moderate SHAPE reactivity (gray). The predicted secondary structures were consistent with SHAPE modification (Fig. S1). Highly modified nucleotides are shown as spheres on the ribbons. (*B*) SASREF rigid-body model of free *rpoS* RNA. (*Left*) Initial output of SASREF with disconnected fragments arranged to satisfy proximity constraints and the experimental SAXS scattering. (*Right*) Final models were built after filling in missing fragments and connecting adjacent RNA modules. (*C*) CORAL rigid-body model of the *rpoS*•Hfq complex, as in *B*.

Table S1. Summary of *rpoS*•DsrA binding constants and annealing rate constants

	DsrA K_d, nM		DsrA annealing rate, min^{-1}		
rpoS	–Hfq	+Hfq	–Hfq (%)	+Hfq, fast (%)	+Hfq, slow (%)
WT	26 ± 2	0.7 ± 0.1	0.026 ± 0.005 (98)	6.3 ± 1.3 (66)	0.06 ± 0.01 (26)
ΔU_5	23 ± 2	0.32 ± 0.04	0.031 ± 0.006 (94)	5 ± 3 (40)	0.07 ± 0.02 (50)

Shown are binding equilibria and rate constants measured by native polyacrylamide gel electrophoresis, based on data in Fig. 3 *C* and *D*. Experiments were without Hfq or with 0.6 μM Hfq monomer. The binding constants were calculated from DsrA titrations; rate constants were obtained from the formation of DsrA•*rpoS* RNA binary complex plus DsrA•*rpoS*•Hfq ternary complex over time. Values ± SD are based on three or more independent trials. Amplitudes of kinetic phases are given in parentheses.

Table S2. SAXS parameters for Hfq protein and rpoS mRNA

		Guinier				Real space					Mass, Da	
Sample	μM	R_g, Å	±	I(0)	±	R_g, Å	±	I(0)	±	R_{max}	SAXS	Nominal
Hfq	42.4	32.3	0.7	1.86E-02	4.6E-04	32.8	0.8	1.90E-02	3.0E-04	110	73,762	66,996
	84.8	33.7	0.9	3.95E-02	5.4E-04	34.0	0.4	3.95E-02	4.0E-04	120	76,975	66,996
	170	34.3	0.6	8.05E-02	6.1E-04	35.2	0.3	8.10E-02	5.0E-04	130	80,271	66,996
Hfq avg		33.6	0.5	4.45E-02		34.2	0.4	4.40E-02	4.0E-04	120	77,332	66,996
rpoS RNA	1.2	63.8	2.0	3.95E-02	1.3E-03	72.0	2.0	4.20E-02	1.2E-03	250	102,027	96,209
	2.3	63.8	1.2	7.80E-02	1.0E-03	71.5	1.4	8.20E-02	1.4E-03	250	105,402	96,209
	4.6	64.2	0.9	1.55E-01	2.0E-03	71.8	0.9	1.64E-01	1.8E-03	250	106,059	96,209
rpoS avg		66.0	1.6	8.97E-02	2.0E-03	76.7	2.7	9.60E-02	2.0E-03	300	106,642	96,209
1:1 Hfq:*rpoS*	2.3	58.0	1.0	1.38E-01	2.1E-03	61.1	0.7	1.40E-01	1.4E-03	250		163,205

SAXS data for Hfq protein, rpoS301 RNA, and 1:1 [Hfq]6:*rpoS* mixtures were acquired at room temperature over a momentum transfer range of $0.005 < q < 1.007$ Å^{-1} at APS 12-ID-B as described in *Materials and Methods*. For the 1:1 complex, the sample contained 2.3 μM RNA and 13.8 μM Hfq monomer. The $P(r)$ real space parameters were calculated for $q = 0–0.5$, using GNOM. The particle mass was estimated from the SAXS scattering curves by the method of Rambo and Tainer (21) for $q = 0–0.3$ to reduce contributions of noise at high q.